Electronic Supplementary Information (ESI) for

A hexangular ring-core $NiCo_2O_4$ porous nanosheet/NiO nanoparticle composite as an advanced anode material for LIBs and catalyst for CO oxidation applications

Yanyan He, Liqiang Xu*, Yanjun Zhai, Aihua Li and Xiaoxia Chen

Experimental Section.

Material synthesis

In a typical procedure, 0.01 mol $Ni(CH_3COO)_2·4H_2O$ and 0.01 mol Co $(CH_3COO)_2·4H_2O$ were dissolved in 20 ml distilled water, the mixture was stirred for 30 min and then 20 ml of NaOH (0.16 g) aqueous solution was added drop wise. Finally the solution was transferred to a Teflon-lined stainless-steel autoclave. After it was stirred vigorously for 1h, the autoclave was heated at 180 ℃ and maintained for 12 h. The resulting precipitates were collected by filtration, washed with distilled water and ethanol for three times, and dried at 60 ℃. To obtain the final products, the as-prepared products were calcined in air at 300, 350, 400, 500 ℃ for 2 h with a heating rate of 1℃/min, respectively.

Structural characterization

X-ray powder diffraction (XRD) patterns of the as-obtained products were achieved on a Bruker D8 advanced X-ray diffractometer ($Cu_{k\alpha}$ radiation, λ=1.5418 Å). The morphologies and sizes of the samples were characterized by transmission electron microscopy (TEM) and scanning electron microscopy (SEM) measurements which were carried out using a JEM-2100 microscope, and a JSM-7600F field-emission microscope. The high resolution images and STEM images were observed on a high resolution transmission electron microscope (HRTEM, JEOL-2011) operating at 200 kV. The BET surface area (SBET) and Barrett-Joyner-Halenda (BJH) pore size distribution (PSD) were measured on a QuadraSorb SI surface area analyzer (version 5.06).

Electrochemical measurements

The electrochemical performances of the samples were tested in 2032-coin cells. The working electrodes consist of active materials (60 wt. %), carbon black (30 wt. %), and carboxymethyl cellulose Ⅲ (CMC) (10 wt. %). Distilled water was used as the solvent. The mixed slurry was then spread onto a copper foil current collector and dried under vacuum at 60°C for 12 h, and then the copper foil was roll-pressed and cut into discs. The final loading density of the active materials was approximately 1-1.5 mg cm^{-2}. Lithium discs with the diameter of 15 mm were used as the counter electrode. The electrolyte is the solution of 1M $LiPF_6$ dissolved in ethylene carbonate/dimethyl carbonate/diethyl carbonate (EC/DMC/DEC, 1:1:1 by volume). The cells were assembled in an argon-filled glove box. Galvanostatic discharge–charge cycling was performed on Land-CT2001A battery cyclers at 25 ℃ and cyclic voltammetry (CV) profile was measured at LK2005A Electrochemical Workstation in the range of 0.01–3V at a scanning rate of 0.1 mV s^{-1}.

CO Oxidation Catalysis

In the catalytic experiments, the activity of the composite was measured using a continuous flow fixed bed micro-reactor, equipped by an electronically temperature programmed tube furnace at atmospheric pressure. The system was first purged with high purity N_2 gas (99.999 %), until the concentration of CO and CO_2 are about 0 ppm, and then a gas mixture of high-purity N_2

(99.999 %, flow rate 32 ml/min), high-purity CO/N_2 mixed gas (10% CO in N_2, 99.999 %, flow rate 4 ml/min) and high-purity O_2 (99.995 %, flow rate 4 ml/min) were introduced into the reactor which contained 50 mg crushed the composites. The concentrations of CO and CO_2 were analyzed by an online infrared gas analyzer (Gasboard-3121, China Wuhan Cubic Co.) and the resolution of the concentrations is 10 ppm.

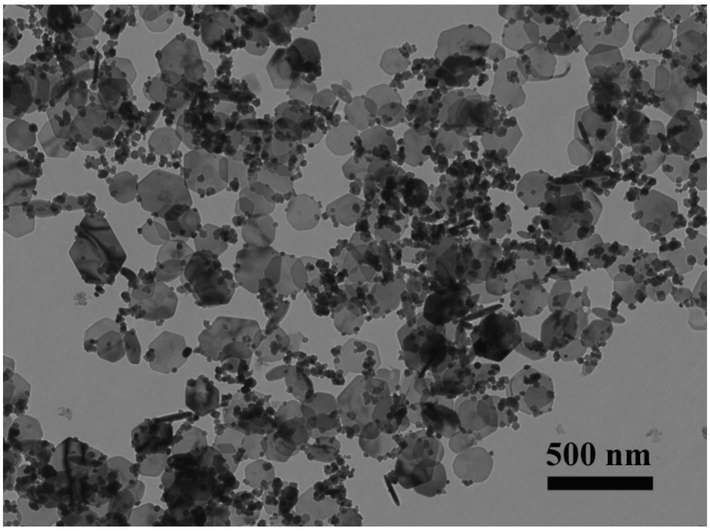

Fig. S1 TEM image of the product obtained after the hydrothermal reaction.

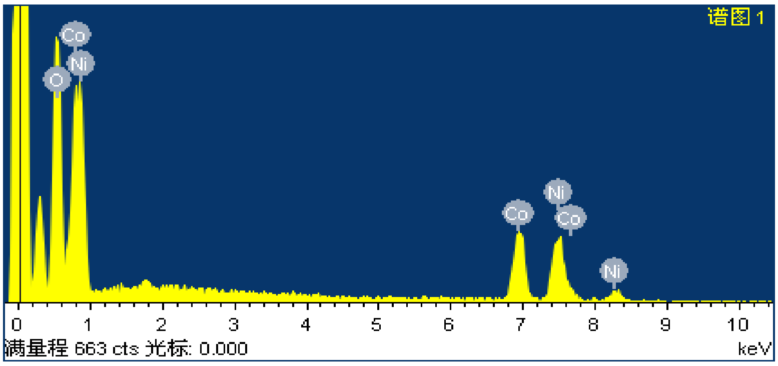

Fig. S2 Energy Dispersive Spectrum (EDS) analysis of the composite.

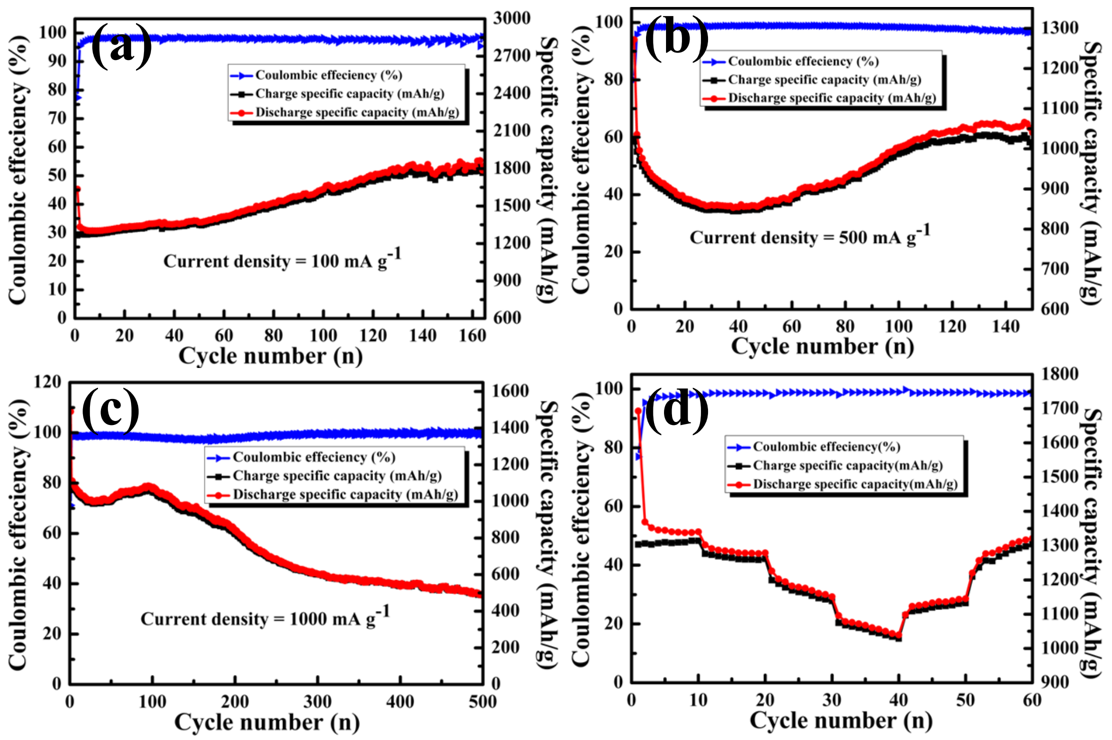

Fig. S3 Cycling performance and coulombic efficiency of the product obtained after the hydrothermal reaction at a current density of 100 mA g^{-1} (a), 500 mA g^{-1} (b), 1000 mA g^{-1} (c) and (d) Rate performance.

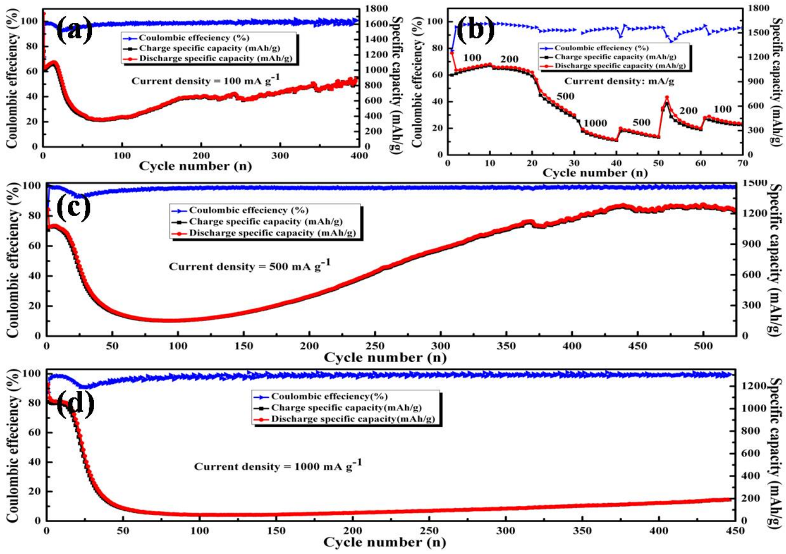

Fig. S4 Cycling performance and coulombic efficiency of the $NiCo_2O_4$/NiO composite at a current density of 100 mA g^{-1} (a), 500 mA g^{-1} (c), 1000 mA g^{-1} (d) and (b) Rate performance.

In addition, the electrochemical performance of the working electrodes which consist of active material (70 wt%), carbon black (20 wt%), and carboxymethyl cellulose III (CMC) (10 wt%) are shown in Fig. S4 (ESI†), and a comparison between a carbon black content of 20 wt% and 30 wt% showed that carbon black could increase the stability of the material. The $NiCo_2O_4/Ni(OH)_2$ nanoparticle composite showed good electrochemical performance which is shown in Fig. S3 (ESI†).

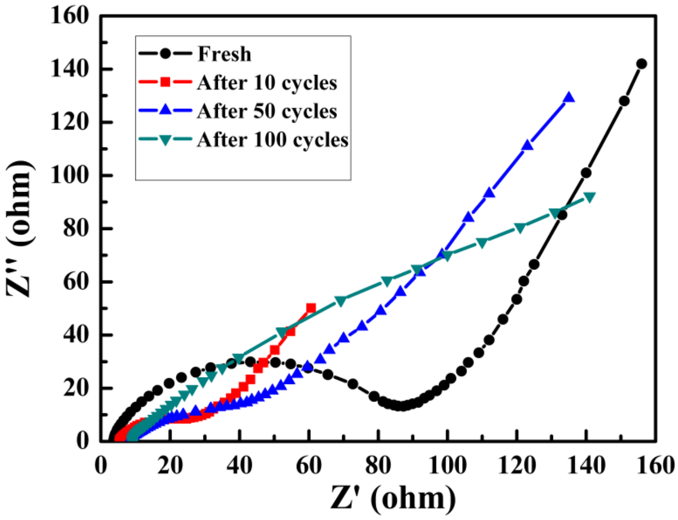

Fig. S5 Electrochemical impedance spectra for the $NiCo_2O_4$/NiO composite cell before and after discharge–charge cycling for 10 cycles，50 cycles, 100 cycles at the current density of 500 mA g^{-1}.

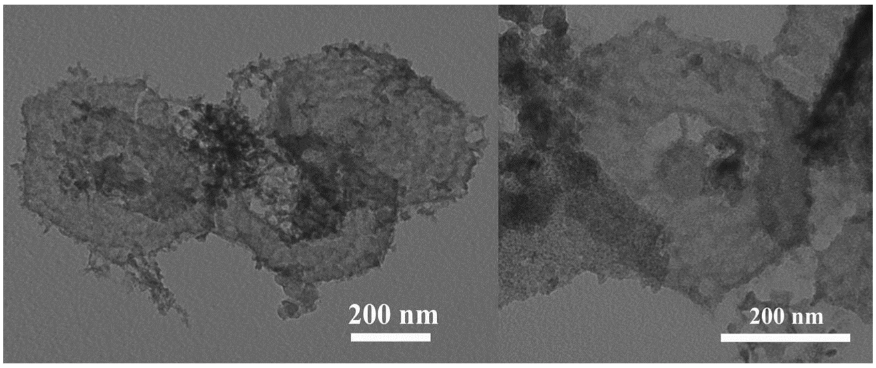

Fig. S6 TEM images of the cycled composite (350 ℃) at a current density of 100 mA g^{-1} after 50 cycles.

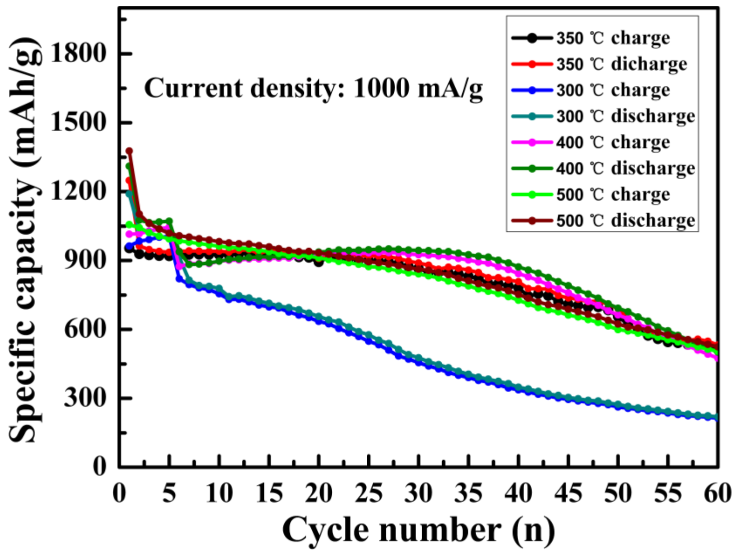

Fig. S7 Cycling performances of the products obtained at different temperature (300 ℃, 350 ℃, 400 ℃, 500 ℃) at a current density of 1000 mA g^{-1}.

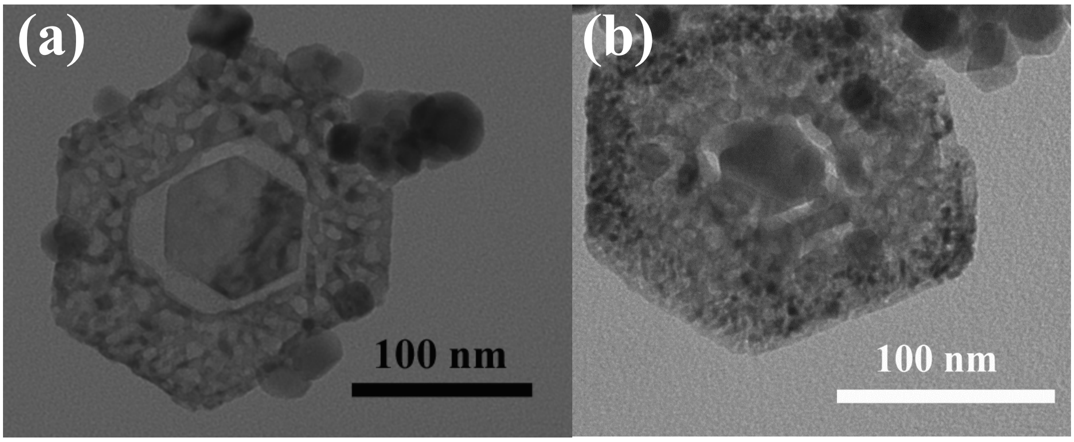

Fig. S8 Randomly selected TEM images of one unit of the composite from the whole (350 ℃) (a) before CO oxidation reaction and (b) after CO oxidation reaction.

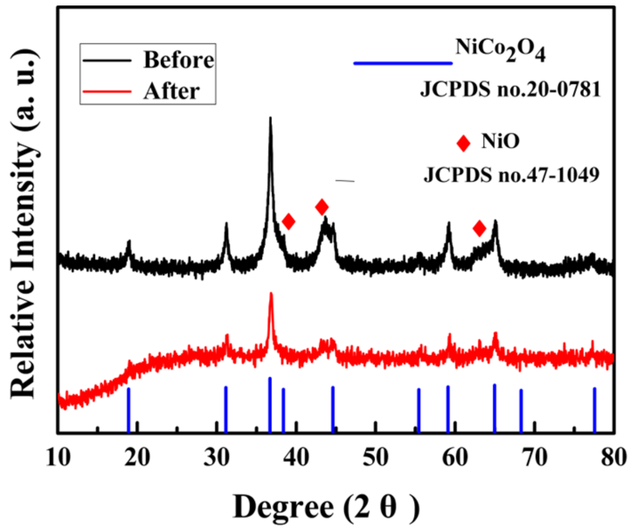

Fig. S9 XRD patterns of the composite (350 °C) before CO oxidation reaction and after CO oxidation reaction.

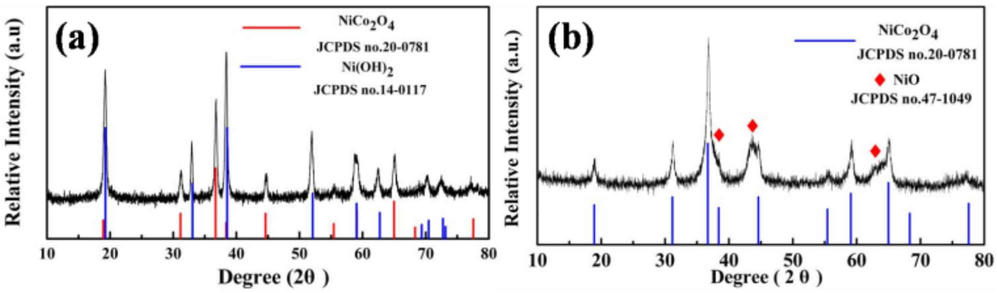

Fig. S10 XRD patterns of (a) the product obtained after the hydrothermal reaction; (b) the products after the calcinations (350 ℃).

Fig. S10 (a) shows the XRD pattern of the product obtained after the hydrothermal reaction and all the diffraction peaks could be indexed to hexagonal $Ni(OH)_2$ (JCPDS card no.14-0117) and cubic $NiCo_2O_4$ (JCPDS card no.20-0781). As shown in Fig. S10 (b), the cubic $NiCo_2O_4$ (JCPDS card no.20-0781) and cubic NiO (JCPDS card no.47-1049) are co-existed in the products after the calcinations process of 350 ℃.

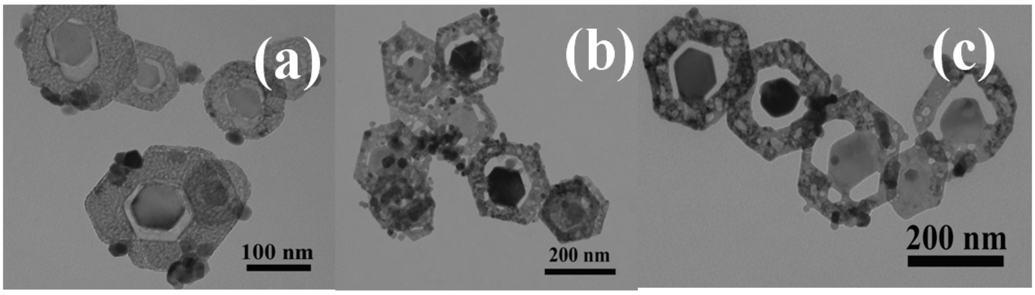

Fig. S11 TEM images of the composite obtained at different calcination temperatures: (a) 300 ℃,(b) 400 ℃, (c) 500 ℃.

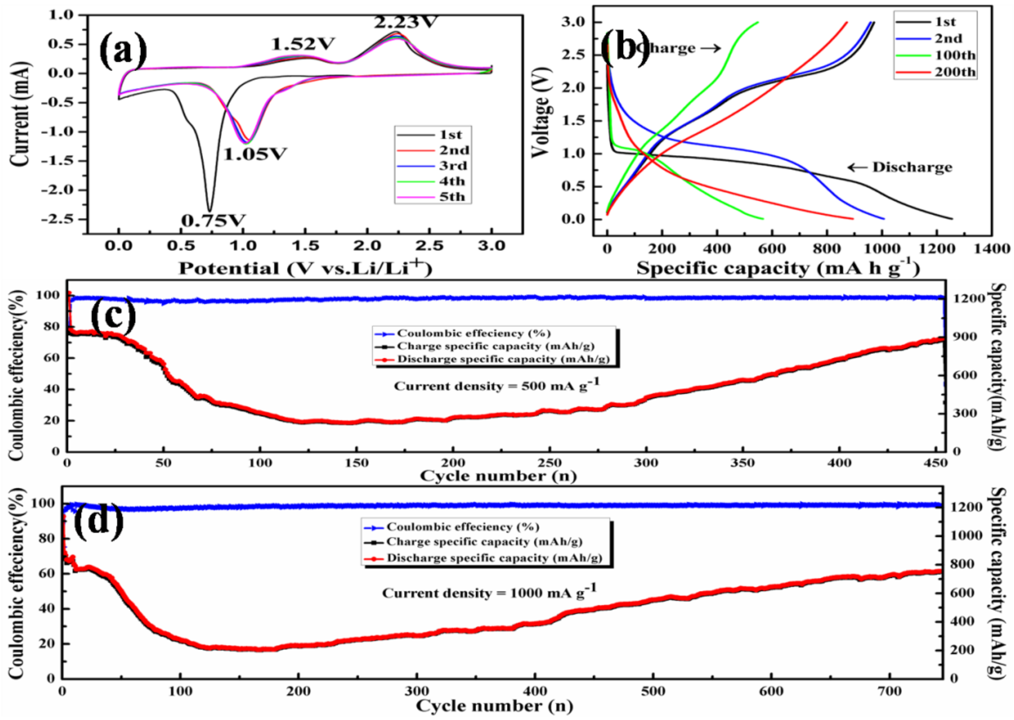

Fig. S12 The CV curves (a);the charge–discharge curves at 200 mA g^{-1} (b); cycling performance and coulombic efficiency at 500 mA g^{-1} (c) and 1000 mA g^{-1} (d) of the composite (350 ℃).

Fig. S12 (a) shows the cyclic voltammograms of the $NiCo_2O_4$/NiO composite for the 1st, 2nd, 3rd, 4th and 5th cycles at a scan rate of 0.1 mV s^{-1} in the voltage window of 0.01–3 V Li/Li$^+$. During the first reduction scan, an intense reduction peak around 0.75 V was observed, which may be assigned to the reduction of $NiCo_2O_4$ to metallic Ni and Co (eqn (1)). Meanwhile, the two oxidation peaks at around 1.5 V and 2.2 V correspond to the oxidation of Ni0 to Ni^{2+} (eqn (2)) and Co to Co^{3+} (eqn (3) and (4)). During the subsequent cycles, the reduction peak shifted to around 1.05 V and the oxidation peaks changed inconspicuously. The CV curves were similar after the first cycle, which suggested that the performance of the electrode is stable. The lithium intercalation and extraction in the reactions might be attributed to the process as follows:[20, 21]

$$NiCo_2O_4 + 8Li^+ + 8e^- \rightarrow Ni + 2Co + 4Li_2O \quad (1)$$

$$Ni + Li_2O \leftrightarrow NiO + 2Li^+ + 2e^- \quad (2)$$

$$Co + Li_2O \leftrightarrow CoO + 2Li^+ + 2e^- \quad (3)$$

$$CoO + 4/3Li_2O \leftrightarrow 1/3Co_3O_4 + 8/3Li^+ + 8/3e^- \quad (4)$$

Table S1 Comparisons between the hexangular ring-core $NiCo_2O_4$ porous nanosheet/NiO nanoparticle composite and previously reported $NiCo_2O_4$ and related nanocomposite.

Electrode materials	Reversible capacity ($mA\ h\ g^{-1}$)	Current density ($mA\ g^{-1}$)	Cycle number (n)	Ref.
$NiCo_2O_4$ porous nanoplates/RGO	816	100	70	1
Fe_2O_3@$NiCo_2O_4$ porous nanocages	1079.6	100	100	2
$NiCo_2O_4$ nanotubes decorated by Au nanoparticles	732.5	100	200	3
$NiCo_2O_4$/C nanocomposite	751.8	40	50	4
Carbon-Coated $NiCo_2O_4$@SnO_2	765	100	50	5
Mesoporous spinel $NiCo_2O_4$	1000	442	400	6
$NiCo_2O_4$ mesoporous microspheres	1198 705	200 800	30 500	7
$NiCo_2O_4$ nanoflakes nanobelts	884 981	500 500	100 100	8
$NiCo_2O_4$ hollow nanospheres	695	200	200	9
$NiCo_2O_4$ hollow nanocubes	1160	200	200	10
$NiCo_2O_4$ microflowers	720	500	100	11
Our work (hexangular ring-core $NiCo_2O_4$ porous nanosheet/NiO nanoparticle composite)	1567.3 894 893 753	100 200 500 100	50 200 455 740	

Table S2 Comparisons between the hexangular ring-core $NiCo_2O_4$ porous nanosheet/NiO nanoparticle composite and previously reported anode materials.

Electrode materials	Reversible capacity (mA h g^{-1})	Current density (mA g^{-1})	Cycle number (n)	Ref.
Graphite	360	53.1	150	12
Porous carbon sphere	365	37.2	100	13
	250	372	100	
N-doped graphene /graphite	344.5	3720	1000	14
Si/C composite	600	100	100	15
Mesoporous Si nanorod	1038	200	170	16
TiO_2 nanowires	292	50	1000	17
	189.8	50	2000	
Nano-$Li_4Ti_5O_{12}$/carbon nanotubes	~150	106.5	100	18
Hierarchical titanate microspheres	~230	50	100	19
Our work (hexangular ring-core $NiCo_2O_4$ porous nanosheet/NiO nanoparticle composite)	1567.3	100	50	
	894	200	200	
	893	500	455	
	753	100	740	

Table S3 Inductively coupled plasma atomic emission spetrometry (ICP-AES) analysis of the composite.

Elem	Avg	Units	Stddev	%RSD
Co 2286	4.145	ppm	.000	.0014
Ni 2316	4.124	ppm	.001	.0.282

In the composite, $NiCo_2O_4$ belongs to cubic system and isostructural to Co_3O_4 with spinel structure, According to the previous reports,[22, 23] Co^{3+} is the active site of the CO oxidation ,the large amount of Co^{3+} cations provide sufficient sites for CO adsorption, which occurs easily. The reaction between the adsorbed CO and the nearby active oxygen species to form CO_2 might be the rate-determining step. Similarly, the NiO belongs to cubic system, Ni^{2+} is the active site of the CO oxide according to the previous report,[24] and the CO adsorbed to Ni-O reacting with the active oxygen species form CO_2.

References:

1 Y. J. Chen, M. Zhuo, J. W. Deng, Z. Xu, Q. H. Li and T. H. Wang, *J. Mater. Chem.* A, 2014, **2**, 4449.

2 G. Huang, L. L. Zhang, F. F.Zhang and L. M. *Wang, Nanoscale*, 2014, **6**, 5509.

3 J. Zhu, Z. Xu and B. A. Lu, *Nano Energy*, 2014, **7**, 114.

4 Y. N. NuLi, P. Zhang, Z. P. Guo, H. K. Liu and J. Yang, *Electrochem. Solid-State Lett.*, 2008, **11**, A64.

5 G. X. Gao, H. B. Wu, S. J. Ding and X. L. Wang, *Small*, 2014, **4**, 432.

6 H. S. Jadhav, R. S. Kalubarme, C. N. Park, J. Kim and C. J. Park, *Nanoscale*, 2014, **6**, 10071.

7 J. F. Li, S. L. Xiong, Y. R. Liu, Z. C. Ju and Y. T. Qian, *ACS Appl. Mat. Interfaces*, 2013, **5**, 981.

8 A. K. Mondal, D. W. Su, S. Q. Chen, X. Q. Xie, and G. X. Wang, *ACS Appl. Mat. Interfaces*, 2014, **6**, 14827.

9 X. Y. Yao, C. Y. Zhao, J. H. Kong, D. Zhou and X. H. Lu, *RSC Adv.*, 2014, **4**, 37928.

10 H. Guo, L.X. Liu, T. T. Li, W. W. Chen, J. J. Liu, Y. Y. Guo and Y. C. Guo, *Nanoscale*, 2014, **6**, 5491.

11 J. M. Xu, L. He, W. Xu, H. B. Tang, H. Liu, T. Han, C. J. Zhang and Y. H. Zhang, *Electrochim. Acta,* 2014, **145**, 185.

12 H. Buqa, D. Goers, M. Holzapfel, M. E. Spahr and P. Novak, *J. Electrochem. Soc.*, 2005, **152**, A474.

13 V. Etacheri , C. W. Wang, M. J. O'Connell, C. K. Chan and V. G. Polet, *J. Mater. Chem. A*, 2015, **3**, 9861.

14 G. H. Wu, R. Y. Li, Z. J. Li, Z. G. Gu and G. L. Wang, *Electrochim. Acta*, 2015, **171**,156.

15 M. Li, X. H. Hou, Y. J. Sha, J. Wang, S. J. Hu, X. Liu and Z. P. Shao, *J. Power Sources*, 2014, **248**,721.

16 Y. L. Zhou, X. L. Jiang, L. Chen, J. Yue, J. Yang and Y. T. Qian, *Electrochim. Acta*, 2014, **127**, 252.

17 F. X. Wu, Z. X. Wang, X. H. Li and H. G. Guo, *J. Mater. Chem.*, 2011, **21**, 12675.

18 H. F. Ni and L. Z. Fan, *J. Power Sources*, 2012, **214**, 195.

19 J. M. Li, W. Wan, F. Zhu, Q. Li, H. H. Zhou, J. J. Li and D. S. Xu, *Chem. Commun.*, 2012, **48**, 389.

20 Y. J. Zhai, H. Z. Mao, P. Liu, X. C. Ren, L. Q. Xu and Y. T. Qian, *J. Mater. Chem. A*, 2015, **3**, 16142.

21. H. S. Jadhav, R. S. Kalubarme, C. N. Park, J. Kim and C. J. Park, *Nanoscale*, 2014, **6**, 10071.

22 J. Jansson, *J. Catal.*, 2000, **194**, 55.

23 X. Xie, Y. Li, Z. Q. Liu, H. Masatake and W. J. Shen, *Nature*, 2009, **458**, 746.

24 C. J. Tang, J. C. Li, X. J. Yao, J. F. Sun, Y. Cao, L. Zhang, F. Gao, Y. Deng and L. Dong, *Appl. Catal., A*, 2015, **494**, 77.